Nano Research

Open Access

Research Article

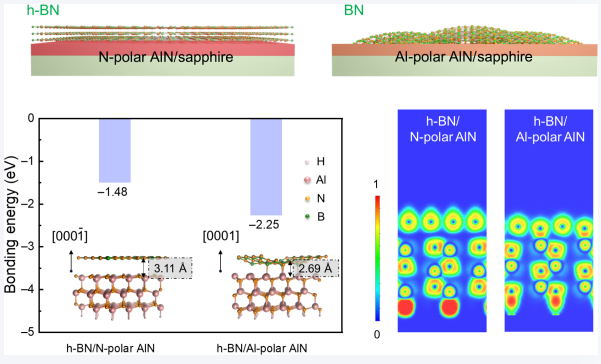
Polarity-guided epitaxy of h-BN on AlN using MOVPE for 2D–3D integration

Yuning Wang[1] ✉, Ryota Akaike[1,2], Kosuke Takagi[1], Tomohiro Tamano[1], Hiroki Yasunaga[2,3], Wentao Zhang[4,5], Ke Xu[4,6,7], and Hideto Miyake[1,2]

[1] *Graduate School of Engineering, Mie University, Tsu 514-8507, Japan*
[2] *Innovation Center for Semiconductor and Digital Future, Mie University, Tsu 514-8507, Japan*
[3] *Organization for Research Initiative and Promotion, Mie University, Tsu 514-8507, Japan*
[4] *Suzhou Institute of Nano-Tech and Nano-Bionics, Chinese Academy of Sciences, Suzhou 215123, China*
[5] *School of Nano-Tech and Nano-Bionics, University of Science and Technology of China, Hefei 230026, China*
[6] *Suzhou Nanowin Science and Technology Co., Ltd., Suzhou 215123, China*
[7] *Jiangsu Institute of Advanced Semiconductors, Suzhou 215123, China*

Cite this article: *Nano Research*, **2026**, *19*, 94908822. https://doi.org/10.26599/NR.2026.94908822

ABSTRACT: Integrating two-dimensional (2D) hexagonal boron nitride (h-BN) with three-dimensional (3D) semiconductor materials offers promising opportunities for multifunctional integrated device architectures. However, direct heteroepitaxy between materials of different dimensionalities remains challenging. Here, the polarity-dependent growth behavior of h-BN films grown by metalorganic vapor phase epitaxy (MOVPE) on AlN/sapphire substrate is reported. The surface polarity of the underlying AlN strongly guides the growth mode of h-BN. On N-polar AlN, h-BN nucleates and grows via van der Waals epitaxy (vdWE), yielding well-oriented 2D films. In contrast, Al-polar AlN promotes interfacial Al–N bond formation, leading to 3D island-type BN growth and a rough morphology. First-principles calculations reveal that N-terminated surfaces spatially and energetically suppress interfacial bonding, whereas Al-terminated surfaces favor strong covalent interactions and significantly larger interfacial binding energies. The crystalline quality of wafer-scale h-BN was further enhanced by high-temperature face-to-face annealing (FFA), achieving a Raman E_{2g} full width at half maximum (FWHM) of 18.3 cm^{-1}. Additionally, composite FFA (CFFA) enabled the fabrication of peelable, flexible AlN films facilitated by the weakly coupled h-BN interface. These results clarify the polarity-driven epitaxial mechanisms of BN on AlN and provide a viable pathway toward scalable 2D–3D hetero-integration and flexible-based nitride electronic and optoelectronic devices.



KEYWORDS: h-BN, AlN, metalorganic vapor phase epitaxy (MOVPE), N-polar, face-to-face annealing

1 Introduction

Hexagonal boron nitride (h-BN) is a wide bandgap (~ 6 eV) two-dimensional material (2DM) with exceptional thermal stability, chemical inertness, and an atomically smooth layered structure [1–3]. These properties make h-BN highly attractive for next-generation electronic, optoelectronic, and photonic devices [4–7]. In van der Waals (vdW) heterostructure transistors, h-BN serves as a high-quality dielectric, encapsulation layer, and ultraflat substrate for charge transport [8–10]. Owing to its chemically inert surface and weak interlayer interactions, h-BN enables remote epitaxy and vdW epitaxy (vdWE) of three-dimensional (3D) semiconductors, facilitating hetero-integration across large lattice mismatches [11–16]. It also functions as an ultrathin buffer layer for preparing high-quality transferable III-nitride films [17, 18].

Chemical vapor deposition (CVD) methods offer a scalable, wafer-level approach for synthesizing high-quality h-BN [6, 19–21]. In comparison with conventional metal-foil growth followed by transfer, direct epitaxy on dielectric or semiconductor substrates eliminates transfer-induced contamination and mechanical damage, resulting in cleaner interfaces. Metalorganic vapor phase epitaxy (MOVPE) has become a highly effective method for the controlled synthesis of h-BN. Due to its wafer-scale uniformity,

Received: January 14, 2026; **Revised:** April 3, 2026
Accepted: May 8, 2026

✉Address correspondence to wang.eng@mie-u.ac.jp

high growth rate, and precise process control, MOVPE allows for the reproducible fabrication of crystalline h-BN with adjustable thickness [22–25]. Most importantly, it exhibits excellent compatibility with established III-nitride growth techniques, facilitating the integration of h-BN within existing nitride-based device platforms [26, 27].

The substrate and its surface properties have a critical influence on the crystallinity and stress state of h-BN growth. Sapphire is the most widely used substrate owing to its availability and thermal stability [5, 28]. However, owing to the large lattice/thermal mismatch, the tendency to form an amorphous BN interlayer at high temperature, and unavoidable oxygen incorporation, collectively disrupt ordered sp^2 BN growth [29]. Diamond (111) shares hexagonal symmetry with h-BN. Yang et al. have successfully grown ordered h-BN films on the diamond (111) surface, while only disordered BN was obtained on the diamond (100) surface [30]. This shows that the atomic arrangement of the substrate surface is crucial to the epitaxial orientation of h-BN. GaN, though hexagonal, suffers thermal decomposition at the typical h-BN growth window (more than 1000 °C), making it difficult to grow smooth, continuous h-BN layers [31]. Consequently, high-quality h-BN for GaN devices is often grown on metal/sapphire and then transferred [32]. In contrast, AlN provides closer lattice/thermal compatibility and excellent thermal stability, establishing it as a promising platform for h-BN growth [33]. However, Yang et al. reported predominantly 3D island-like BN growth on Al-polar AlN, which disrupts the formation of high-quality layered h-BN films [34]. Notably, when h-BN is grown on 2DMs like graphene, the weak vdW interface promotes layer-by-layer growth and highly oriented h-BN, suggesting that vdW interfaces could be an effective approach [35].

In this work, we epitaxially grew h-BN films on N-polar AlN substrates using MOVPE with a pulsed growth method. Unlike conventional Al-polar AlN surfaces, N-polar AlN surfaces are terminated with N atoms. This surface polarity greatly influences the nucleation and growth of h-BN. Combining first-principles calculations with experimental characterization, how N-terminated surfaces inhibit interfacial bonding is revealed. Due to the short covalent bond length and high bond energy of B–N, its formation on N-terminated surfaces is spatially and energetically limited, making the formation of strong chemical bonds more difficult compared to Al-terminated surfaces. As a result, N-polar AlN favors the formation of sp^2-hybridized h-BN, promoting 2D growth. Face-to-face annealing (FFA) effectively reduces defects and improves order, producing highly oriented h-BN films with sharper X-ray diffraction (XRD) diffraction peaks and narrower Raman full width at half maximum (FWHM). Moreover, composite FFA (CFFA) enables exfoliation of flexible, low-stress AlN films via the weakly coupled h-BN interface. This highlights its potential for achieving low-stress, high-quality 2D–3D integration in nitride semiconductors.

2 Results and discussion

To start, Al-polar and N-polar AlN template substrates were prepared on sapphire substrates using sputtering and FFA (FFA sp) techniques, as previously reported [36–39]. These AlN templates exhibit high crystal quality and smooth surfaces, which facilitate subsequent h-BN epitaxial growth (Table S1 and Fig. S1 in the Electronic Supplementary Material (ESM)). Next, h-BN was epitaxially grown on AlN templates with different polarities using MOVPE. Prior to growth, the substrates were thermally cleaned in H_2/NH_3 ambient at 1300 °C for 10 min to remove surface oxides (Figs. 1(a) and 1(d) and Fig. S2 in the ESM). After cleaning, both N-polar and Al-polar AlN surfaces remained atomically flat with step-and-terrace morphologies (root-mean-square (RMS) roughness = 0.3 nm), which is favorable for subsequent h-BN epitaxy (Figs. 1(b) and 1(e)). h-BN was then directly grown on the AlN templates using a pulsed growth scheme with alternating triethylboron (TEB)/NH_3 pulses (t(TEB)/t(NH_3) = 2 s/1 s, where t denotes the pulse duration). The flow rates of NH_3 and TEB were 89.2 mmol/min and 14.8 μmol/min, respectively, corresponding to a V/III ratio of approximately 6000. Growth occurred at 1400 °C under a total pressure of 30 Torr with H_2 as the carrier gas (Fig. S2 in the ESM). The nucleation layers grown for 2 min on the two polarities of AlN are shown in Fig. S3 in the ESM. On N-polar AlN, h-BN tends to grow in a 2D manner, forming atomically flat surfaces. Conversely, on Al-polar AlN, a granular morphology develops, indicating a fundamental difference in the initial growth mode of BN on the two types of polarity templates. By extending the growth time to 30 min, h-BN films with a thickness of more than 10 nm were obtained on both N-polar and Al-polar AlN templates. Atomic force microscopy (AFM) image reveals that the N-polar surface exhibits low RMS roughness (1.92 nm), characterized by a relatively smooth surface and distinctive wrinkle-like features (Fig. 1(c)) [40, 41]. In contrast, the Al-polar surface exhibits continued 3D island-like growth with a significantly rougher morphology, characterized by an RMS of 12.94 nm (Fig. 1(f)). Raman spectroscopy is a straightforward method for material identification, further confirming the formation of sp^2-hybridized BN [42, 43]. The characteristic E_{2g} phonon mode of h-BN, originating from the in-plane opposite vibrations of B and N atoms in the hexagonal lattice, and characteristic E_{2g} peaks were observed in both samples (Fig. 1(g)). XRD analysis reveals that the h-BN (0002) reflection at ~ 26.5° was observed for the N-polar sample (Fig. 1(h)), which is consistent with the commonly reported peak position for MOVPE-grown h-BN (typically 26.5° to 26.7°) [28, 30, 34]. This peak shift relative to the standard peak position is attributed to the coexistence of turbostratic BN (t-BN) domains and residual strain within the film. However, no characteristic h-BN (0002) diffraction peak is observed for the BN grown on Al-polar AlN, indicating its poor c-axis orientation (Fig. 1(i)). In addition, XRD analysis of the N-polar AlN and Al-polar AlN templates prior to growth was used for comparison (Fig. S4 in the ESM), demonstrating that only the h-BN (0002) peak appeared after growth, with no other BN peaks observed. This confirms the growth of well-oriented h-BN on N-polar AlN.

To further investigate the reasons for the differential growth of BN on AlN substrates of different polarities, cross-sectional transmission electron microscopy (TEM) specimens of BN on AlN of varying polarities were prepared (Fig. 2 and Figs. S5 and S6 in the ESM). The differing polarities of the AlN substrates were further confirmed by atomic imaging. The Al-polar AlN exhibits a typical inversion domain boundary (IDB) at the interface, reversing from its initial N-polarity to Al-polarity (Fig. S6 in the ESM). Interestingly, h-BN bubbling was observed on N-polar AlN (Figs. S5(a) and S5(b) in the ESM). This phenomenon arises from h-BN bubbles induced by water decomposition during focused ion beam (FIB) sample preparation, triggered by the electron beam from the scanning electron microscopy (SEM) [44]. Conversely, no such

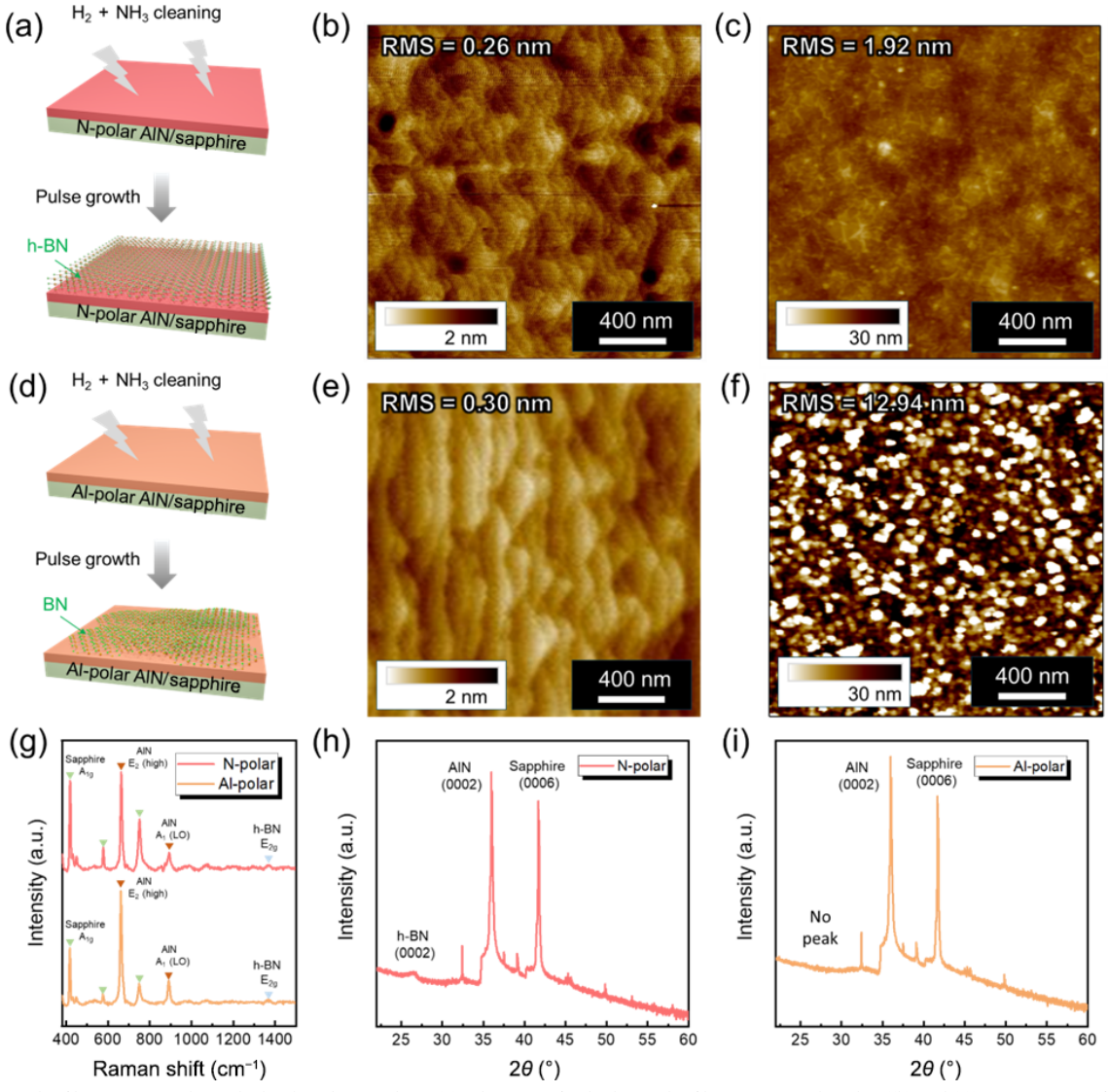


Figure 1 Growth of h-BN on N-polar and Al-polar AlN templates. (a) Schematic of pulsed growth of h-BN on N-polar AlN. ((b) and (c)) AFM images of N-polar AlN (b) after surface cleaning and (c) after the growth of h-BN films. (d) Schematic of pulsed growth of h-BN on Al-polar AlN. ((e) and (f)) AFM images of Al-polar AlN templates (e) after surface cleaning and (f) after the grown h-BN films on Al-polar AlN. (g) Raman spectra of h-BN grown on AlN with different polarities. The green, brown, and blue inverted triangles in the figure correspond to the characteristic peaks of sapphire, AlN, and h-BN. ((h) and (i)) XRD 2θ–ω scans of h-BN grown on (h) N-polar AlN and (i) Al-polar AlN.

bubbling was observed on Al-polar AlN (Fig. S6(a) in the ESM). This may be attributed to the weaker adhesion of h-BN to the N-polar AlN, where cooling-induced strain generates characteristic wrinkling patterns (Fig. 1(c)). Bubble formation represents a mode of localized relaxation strain wrinkling. This observation indirectly corroborates the distinct growth models of BN on AlN substrates of differing polarities.

High-resolution TEM (HRTEM) was employed to characterize the microstructure and orientation of h-BN, as the B atom is difficult to observe due to the high-angle annular dark-field (HAADF) image being proportional to atomic number Z^2. On N-polar AlN, cross-sectional HRTEM clearly resolves layered h-BN parallel to the interface, with an interlayer spacing of approximately 0.33 nm (Fig. 2(a)). The corresponding fast Fourier transform (FFT) pattern reveals an $(0001)[1\bar{1}00]_{\text{h-BN}}\|(000\bar{1})[1\bar{1}00]_{\text{AlN}}$ orientation, indicating a favorable epitaxial relationship between h-BN and AlN (Fig. 2(b)). The energy dispersive X-ray spectroscopy (EDS) line scan along the axial direction further confirms the presence of epitaxial h-BN (Fig. 2(c)). In stark contrast, BN on Al-polar AlN exhibits 3D island-like stacking (Fig. 2(d)). These disordered BN layers stack in an interleaved manner from the beginning, with larger areas becoming affected as growth time increases. The BN FFT exhibits broadened or weakly ring-like features, whereas the AlN diffraction remains sharp (Fig. 2(e)), indicating in-plane and out-of-plane orientation disorder in BN. Corresponding EDS line scans similarly confirm the epitaxial growth of BN on Al-polar AlN (Fig. 2(f)). Furthermore, the transition layer at the interface between h-BN and N-polar AlN was identified as an AlN oxide layer ($Al_xO_yN_z$) rather than a B-containing oxide layer (Fig. S7 in the ESM). This layer primarily results from the separation of h-BN from N-polar AlN, caused by water decomposition triggered by the SEM electron beam during FIB sample preparation [44], which subsequently leads to oxidation of the surface AlN. Oxygen impurities in the TEB source may be

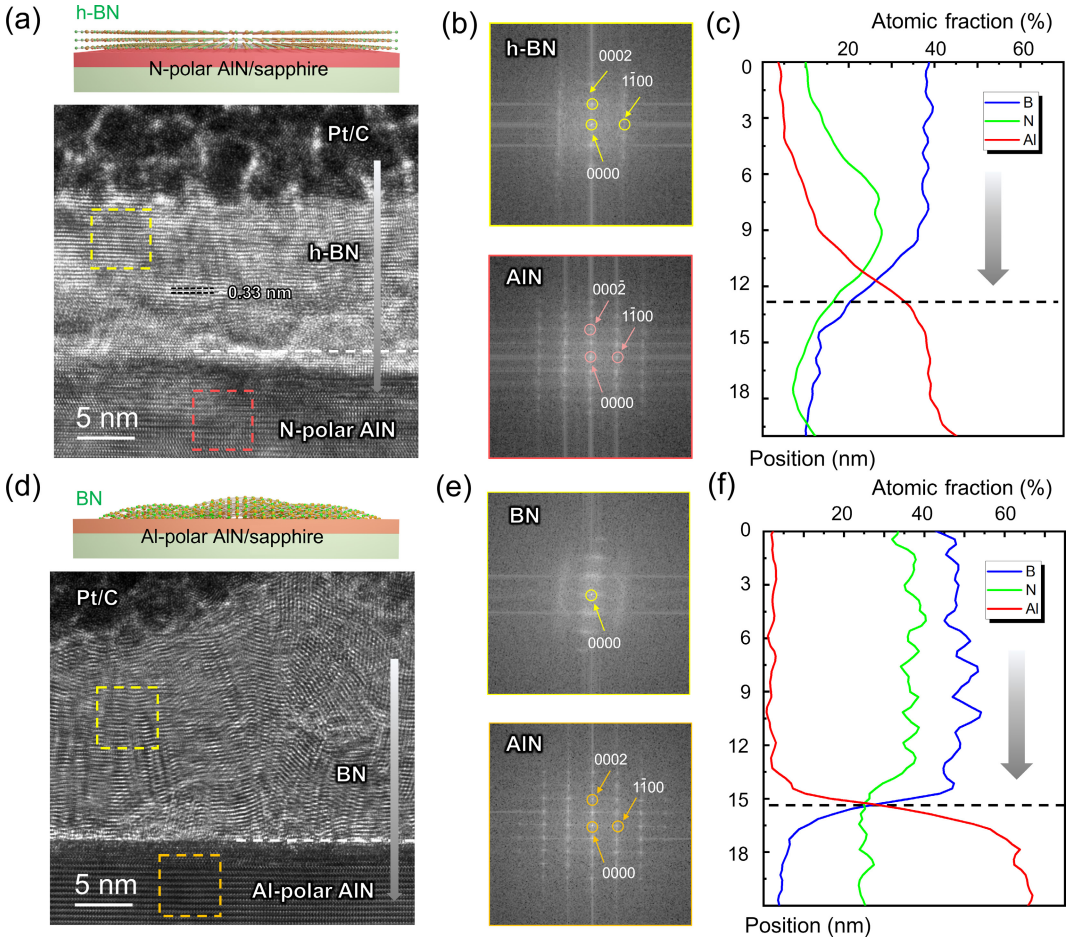


Figure 2 Interface microstructures of BN grown on AlN templates of different polarities. (a) Cross-section schematic and HRTEM image of h-BN/N-polar AlN. The yellow and red boxes denote FFT pattern sampling regions. (b) FFT patterns of the h-BN region (yellow box) and AlN region (red box) in (a), labeled $(0001)[1\bar{1}00]_{h\text{-}BN}\|(000\bar{1})[1\bar{1}00]_{AlN}$. (c) Intensity profile of EDS signals for B, N, and Al atoms at the interface along the vertical grey arrow in (a). (d) Cross-section Schematic and HRTEM of BN/Al-polar AlN. The yellow and orange boxes denote FFT pattern sampling regions. (e) FFT patterns of the BN region (yellow box) and AlN region (orange box) in (d). BN exhibits broadened and ring-like features, whereas AlN shows sharp diffraction, confirming the disorder orientation of BN. (f) Intensity profile of EDS signals for B, N, and Al atoms at the interface along the vertical grey arrow in (d).

another contributing factor, but the former mechanism is the dominant reason.

To further elucidate the pronounced differences in h-BN growth behavior on AlN surfaces with different polarities, first-principles calculations were performed. Figure 3(a) compares the relaxed interface configurations of h-BN on N-polar and Al-polar AlN substrates. For the N-polar substrate, the average interlayer spacing expanded from 3.0 to 3.11 Å with no covalent bonds observable, indicating the interface is predominantly governed by van der Waals forces. Conversely, on the Al-polar AlN, the average interlayer spacing shortened to 2.69 Å, while covalent bonds formed between B and Al atoms at the interface. Density functional theory (DFT) calculations reveal that the interface binding energy (IBE (E_b)) of h-BN on Al-polar AlN is approximately 1.5 times that on N-polar AlN (Fig. 3(a) and see details in Section S3 Supplementary document in the ESM), indicating stronger interfacial interactions. Electron localization functions (ELFs), which quantify the probability distribution of electrons near the reference electron, distinguish between localized (covalent and ionic) and non-localized (metallic and vdW) bonding states [45]. ELFs further reveal polarity-dependent bonding characteristics (Figs. 3(b) and 3(c)). The N-polar interface shows low localization at the vdW gap, indicating weak bonding. In contrast, strong electron localization between N and Al atoms at the Al-polar interface confirms electron sharing and covalent bond formation.

Bader charge analysis further reveals opposite charge transfer behavior (Fig. 3(d)). h-BN on N-polar AlN loses approximately 0.491e, whereas h-BN on Al-polar AlN gains approximately 1.073e. This redistribution of opposite charges not only alters the electronic properties of h-BN but also reflects stronger interfacial coupling under Al-polar conditions. To more intuitively visualize this polarity-dependent charge transfer, charge density difference (CDD) and the plane-averaged CDD as a function of position z across the interface ($\Delta\rho(z)^{avg}$) were further calculated (Figs. 3(e) and 3(f) and see details in Section S3 Supplementary document in the ESM). Pink and blue regions denote charge accumulation and depletion, respectively. At the Al-polar interface, pronounced accumulation (pink) and depletion (blue) zones emerge between h-BN and AlN, forming strong charge vibrations that confirm the formation of robust covalent bonds. In contrast, the N-polar interface exhibits only weak charge redistribution consistent with vdW coupling characteristics.

In summary, the N-terminated surface of N-polar AlN exerts an inhibiting effect on interfacial bonding. The formation of B–N

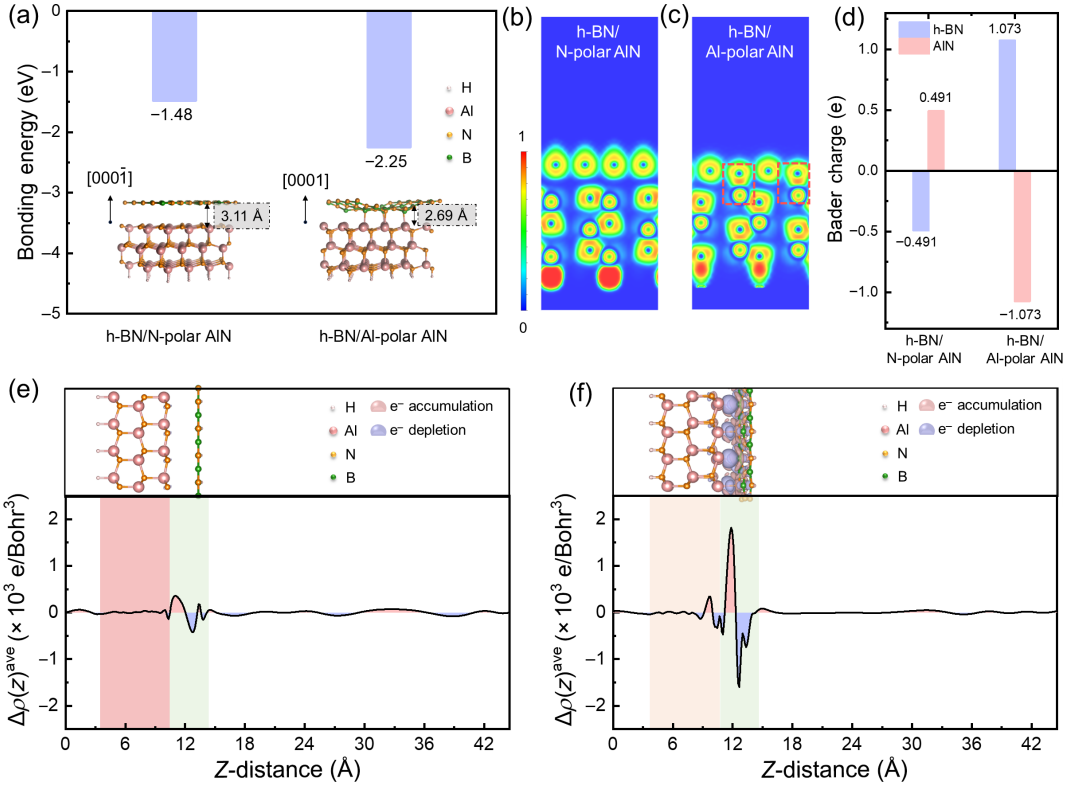


Figure 3 Polarity-dependent interfacial properties at the h-BN/AlN interface. (a) The interface binding energy (IBE) of h-BN on Al-polar AlN and N-polar AlN. The insets show relaxed interfacial structures, with an equilibrium spacing of ~ 3.11 Å for N-polar AlN and 2.69 Å for Al-polar AlN. ((b) and (c)) ELF map of (b) h-BN/N-polar AlN and (c) h-BN/Al-polar AlN. (d) Bader charge analysis of h-BN/AlN heterostructure. ((e) and (f)) CDD images and $\Delta\rho(z)^{avg}$ of (e) h-BN/N-polar AlN and (f) h-BN/Al-polar AlN. The CDD is depicted at isosurface levels of ±0.004 e/Bohr^3.

covalent bonds, characterized by shorter bond lengths and higher bond energies, is spatially and energetically constrained on N-terminated surfaces. Whereas Al atoms on Al-polar AlN surfaces readily form covalent bonds with N atoms at the interface between Al-polar AlN and h-BN, exhibiting higher interfacial bonding energies and substantial charge transfer (Table S2 in the ESM). This leads to the 3D island-like growth of structurally disordered BN.

The FFA process was first introduced by our group [36]. Through solid-phase reactions at high temperatures, it effectively enhances the crystalline quality of AlN, whether deposited by sputtering or epitaxial growth [37, 46–48]. Recently, this technique has also been applied to improve the crystalline quality of h-BN grown on sapphire substrates [18]. Growing h-BN on AlN substrates offers the advantage that AlN remains more stable than sapphire at temperatures up to 1700 °C, preventing h-BN degradation caused by oxygen released from substrate decomposition [49]. This renders FFA a promising method for the efficient and low-cost preparation of high-quality h-BN. As a result, BN grown on AlN substrates of different polarities was subjected to FFA at 1650 °C for 3 h (Fig. 4(a)).

Following annealing, the h-BN on N-polar AlN (designated FFA-hBN) retained its pre-annealing excellent surface roughness (RMS = 1.98 nm), as shown in Fig. 4(b). There was no evidence of poor surface morphology affected by oxygen diffusion. Raman spectroscopy characterized the h-BN E_{2g} peak at 1366 cm^{-1}. The FWHM of the E_{2g} mode, obtained by Lorentzian fitting, was only 18.29 cm^{-1} after annealing, significantly lower than the typical FWHM (20–45 cm^{-1}) for h-BN prepared by MOVPE (Fig. 4(c) and Table S3 in the ESM). It indicates the formation of h-BN with improved interlayer ordering. XRD further revealed enhanced out-of-plane ordering in FFA-BN. The XRD 2θ–ω scan, where ω denotes the incident angle of the X-ray beam with respect to the sample surface, exhibited the h-BN (0002) reflection peak (Fig. 4(d)), positioned closer to the standard peak relative to the pre-annealed state (Fig. 4(g) and Table S4 in the ESM) [28]. Additionally, the h-BN (0004) reflection peak became visible. This indicates that annealing reduced structural defects in BN and improved in-plane crystallinity. The chemical composition and bonding environment were further analyzed via X-ray photoelectron spectroscopy (XPS) (Figs. 4(e) and 4(f)). Full-spectrum scans revealed B, N, and Al signals alongside minor C and O signals. The XPS fine spectra of the B 1s and N 1s peaks were characterized, with the main B 1s peak positioned at 190.15 eV and the main N 1s peak at 397.75 eV, both in good agreement with characteristic B–N bond energies [50, 51]. The absence of additional shoulder peaks indicates that FFA treatment does not introduce unwanted phases or oxides, thereby maintaining chemical stability while enhancing crystalline quality. Notably, however, the surface morphology of BN on Al-polar AlN deteriorated further (RMS increasing from 12.94 to 16.78 nm) (Fig. S8(a) in the ESM). The FWHM of the E_{2g} mode, obtained by fitting Lorentzian functions, was 30.27 cm^{-1} after annealing, substantially larger than that on N-polar AlN (Fig. S8(b) in the ESM). Moreover, the XRD 2θ–ω scan still shows no characteristic peak for h-BN (0002) (Fig. S8(c) in the ESM). This indicates that even after subsequent high-temperature annealing, it was inefficient to enhance the in-plane order of MOVPE BN to obtain 2D h-BN if it followed 3D growth. Furthermore, BN grown on Al-polar AlN

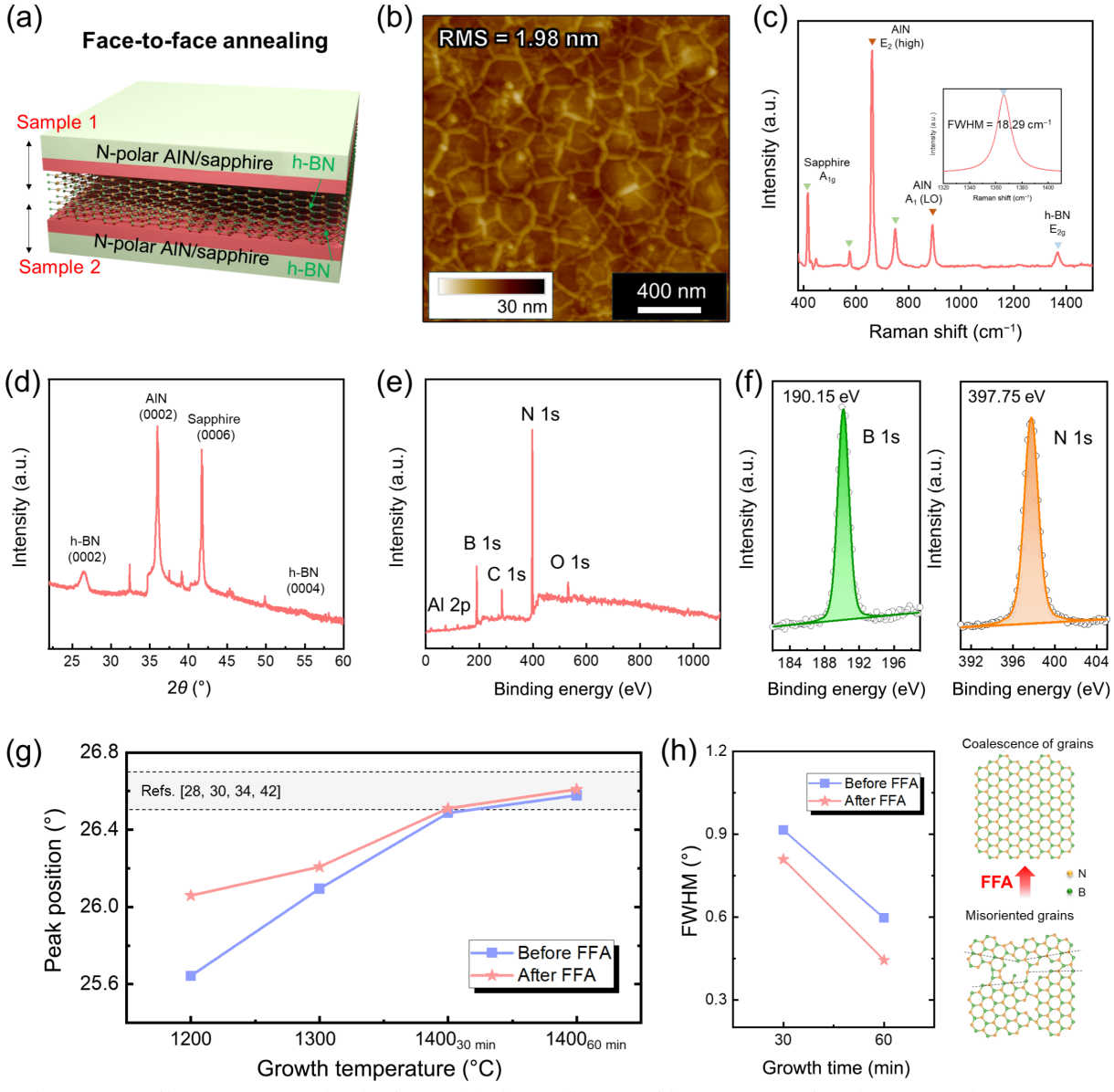


Figure 4 Characterization of h-BN grown on N-polar AlN after FFA. (a) Schematic illustration of the FFA process performed at 1650 °C on h-BN grown on N-polar Al templates. (b) AFM image of the FFA-hBN surface showing an RMS roughness of ~ 1.98 nm. (c) Raman spectrum of FFA-hBN. The green, brown, and blue inverted triangles in the figure correspond to the characteristic peaks of sapphire, AlN, and h-BN. (d) XRD 2θ–ω scan of FFA-hBN. (e) XPS survey spectrum of FFA-hBN. (f) B 1s core-level spectrum and N 1s core-level spectra, confirming stoichiometric h-BN composition and chemical stability after annealing. (g) Evolution of 2θ peak positions before and after FFA at different growth temperatures. (h) The FWHM of the 2θ peak before and after FFA at different growth times at 1400 °C, along with a schematic illustration showing that FFA reduces disorder and improves crystallinity.

surfaces was characterized by XPS (Fig. S9 in the ESM). The B 1s and N 1s energies were located at 190.10 and 397.69 eV, respectively, slightly lower than those on N-polar AlN. This indicates greater B–N stability in h-BN grown on N-polar AlN [33]. For comparison, h-BN grown on sapphire substrates was also measured (Fig. S10 in the ESM). The XPS B 1s peak was obtained by etching from the outermost surface towards the interface, revealing peaks corresponding to the etching duration. This demonstrates that the presence of AlN suppresses the formation of B–O bonds, thereby preventing the emergence of amorphous B-containing layers similar to those observed on sapphire substrates [29].

Furthermore, the crystalline quality of h-BN exhibits a significant positive correlation with growth temperature. When the growth temperature increased from 1200 to 1400 °C, the surface roughness decreased markedly (Figs. 1(c) and 4(b) and Fig. S11 in the ESM). The h-BN (0002) peak position progressively approached the h-BN reference value, accompanied by a decrease in FWHM, which reflected enhanced interlayer order (Figs. 4(g) and 4(h) and Figs. S12–S14 and Table S4 in the ESM) [28, 30, 34, 42]. Although FFA process partially enhances h-BN crystalline quality (Fig. 4(g)), BN grown at lower temperatures remains prone to forming t-BN rather than h-BN due to insufficient atomic migration. This indicates that elevated growth temperatures are crucial for achieving epitaxial h-BN growth on N-polar AlN surfaces via MOVPE. By extending the growth time, approximately 25 nm of h-BN was grown on N-polar AlN at 1400 °C. It also exhibits excellent surface roughness and interlayer order (Figs. 4(g) and 4(h) and Figs. S14–S16 and Table S4 in the ESM).

It has also been reported that FFA in a nitrogen atmosphere promotes vacancy-mediated defect healing and reduces impurity-related defect states [49]. In summary, h-BN grown on N-polar AlN can effectively reduce structural defects, such as stacking faults, grain boundaries, and vacancies, through further FFA processing, and is expected to reduce impurity-related defect states, ultimately enhancing lattice order (Fig. 4(h)). Moreover, this effect applies to h-BN layers of varying thickness. Given that the number of h-BN layers grown via MOVPE can be readily adjusted by modifying the growth time (Fig. S17 in the ESM), this study provides an effective, low-cost strategy for the large-scale preparation of high-quality h-BN layers with different thicknesses.

Finally, flexible AlN films prepared on h-BN via a CFFA process are demonstrated. Specifically, h-BN was grown at 1400 °C for 30 min on AlN of varying polarities, followed by sputtering approximately 300 nm of AlN on top of it. Further, CFFA was employed to simultaneously anneal both sputtered AlN (Sp-AlN) and h-BN at 1650 °C for 3 h. The HRTEM results confirm that the layered structure of h-BN is well preserved after FFA treatment, with a clearer layered structure and fewer structural defects (Fig. S18 in the ESM). No undesirable amorphization, decomposition, or severe lattice disruption was observed at either the h-BN or h-BN/N-polar AlN interfaces. EDS analysis confirmed that there was no significant mutual diffusion of Al and B at the interface after annealing (Fig. S19 in the ESM). This phenomenon is commonly observed in h-BN grown on sapphire [52]. Owing to the well-layered structure of h-BN grown on N-polar AlN, the AlN layer on h-BN/N-polar AlN could be readily exfoliated using ultraviolet (UV) adhesive tape (Fig. 5(a)). In contrast, it was difficult to exfoliate the layer on BN/Al-polar AlN due to the 3D growth structure of BN (Fig. S20 in the ESM). AFM characterization revealed the typically wrinkled morphology of h-BN on both the backside of the exfoliated AlN film and the substrate surface (Figs. 5(b) and 5(c)). Also, XRD 2θ–ω scans and Raman characterization of the exfoliated substrate confirmed the presence of h-BN on the substrate surface (Fig. 5(d) and Fig. S21 in the ESM). This is because the IBE between h-BN/h-BN (E_b = ~ 32 meV/Å^2) is 1/8 to 1/5 of that between AlN/h-BN (Fig. 3(a)) [53]. Consequently, the peeling occurs between h-BN layers, and h-BN maintains a flat surface morphology, offering the possibility of substrate reuse. The exfoliated, flexible AlN film was characterized by HRXRD 2θ–ω scans at the (0002) reflection, as shown in Fig. 5(e), indicating a near-stress-free state. Raman spectroscopy of the AlN film and substrate before and after exfoliation similarly demonstrated that AlN prepared on h-BN exhibits significantly reduced compressive stress compared to FFA Sp-AlN template substrates (Fig. S22 in the ESM). This demonstrates that the h-BN interlayer effectively modulates strain within AlN, holding significant implications for the growth of strain-free and exfoliable III-nitride films and devices.

3 Conclusions

In summary, we have achieved the growth of high-quality h-BN on N-polar AlN templates via the pulse growth method using MOVPE. N-polar AlN promotes layer-by-layer growth of well-oriented h-BN through suppression of interfacial bonding, while Al-polar AlN induces strong interfacial coupling that results in 3D island-like BN formation. Combined with DFT calculations, the differences in polarity-induced BN growth models are revealed. The

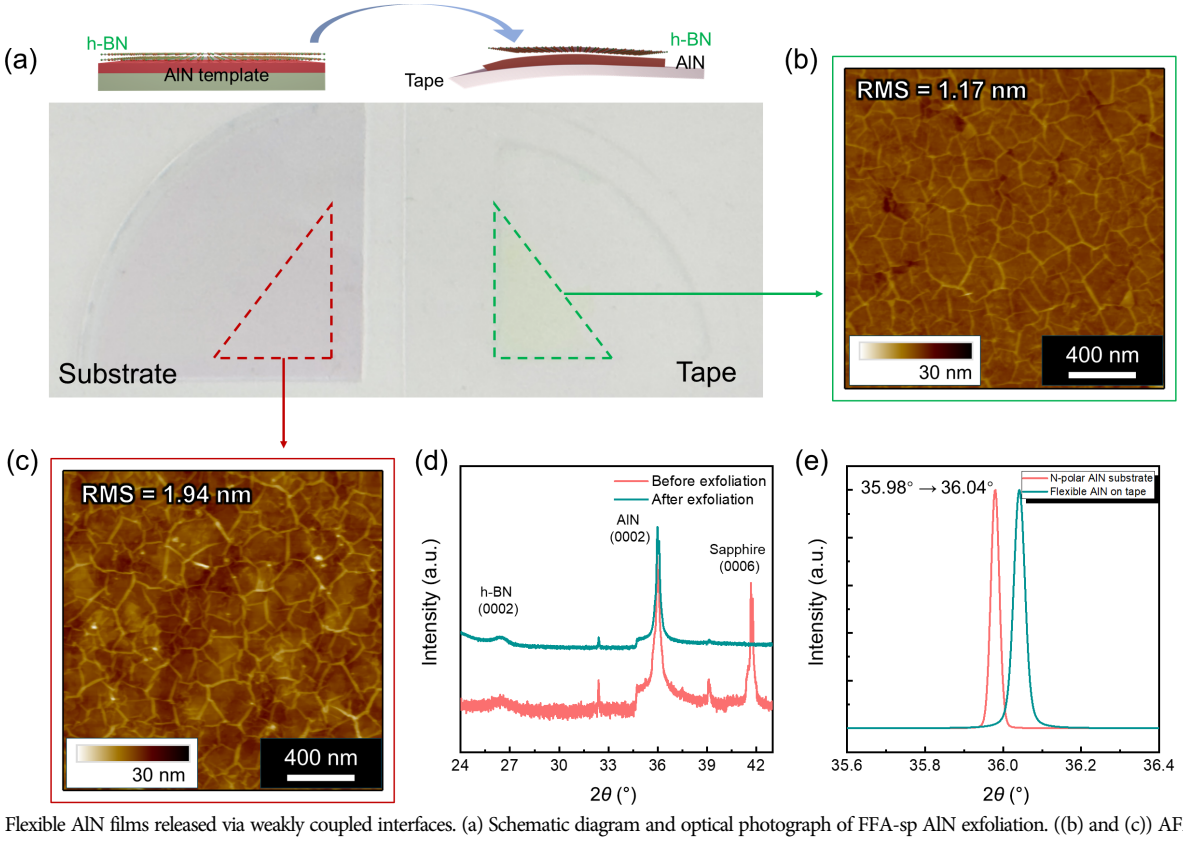


Figure 5 Flexible AlN films released via weakly coupled interfaces. (a) Schematic diagram and optical photograph of FFA-sp AlN exfoliation. ((b) and (c)) AFM images of (b) the flexible AlN backside and (c) the AlN template substrate surface after exfoliation, both displaying h-BN with wrinkled features. (d) XRD 2θ–ω scans of the sample before and after exfoliation. (e) HRXRD (0002) 2θ–ω scan of the substrate and AlN film after exfoliation, demonstrating the nearly stress-free state of AlN film.

termination of the N-polar AlN surface with N atoms energetically and spatially inhibits the formation of $B_{(BN)}$–$N_{(AlN)}$ covalent bonds, thus favoring layer-by-layer growth of h-BN during the initial growth stage. Conversely, Al-terminated surfaces on Al-polar AlN induce bonding between $N_{(BN)}$ and $Al_{(AlN)}$, driving the formation of 3D island-like BN and a rough morphology. FFA effectively reduced defects and improved order in h-BN, achieving highly oriented films with a narrower FWHM Raman E_{2g} (~ 18.3 cm^{-1}). Finally, stress-free flexible AlN films were fabricated using CFFA technology, demonstrating the potential of h-BN grown on N-polar AlN as an effective stress-relief and peel-off buffer layer. This work provides a simple and effective approach for fabricating wafer-scale h-BN with controllable layer numbers, transferable nitride films, and 2D–3D integration.

4 Experimental

4.1 Preparation of AlN template substrates

Both N-polar and Al-polar AlN template substrates were fabricated on 2-inch sapphire substrates with a *c*-axis offset of approximately 0.2° toward the *m*-direction. Specifically, about 300 nm of N-polar AlN was deposited on the sapphire substrate using a high-purity aluminum target (99.9999%). This N-polar AlN layer was deposited via radio frequency (RF, 13.56 MHz) magnetron sputtering at 600 °C, with a sputtering pressure of 0.1 Pa and a nitrogen flow rate of 50 sccm, achieving a deposition rate of roughly 0.05 nm/s. Subsequently, FFA was performed at 1650 °C for 3 h. An approximately 450 nm Al-polar AlN layer was deposited at 600 °C using a sintered AlN target with 99.9% purity. Sputtering was carried out at a pressure of 0.05 Pa and an N_2 flow rate of 24 sccm. The deposition rate of the Al-polar layer was about 0.05 nm/s. After sputtering the Al-polar AlN, FFA was performed at 1700 °C for 3 h to enhance its crystallinity.

4.2 Epitaxial growth of layer-controllable h-BN

h-BN was grown via pulse growth method using MOVPE. Initially, a thermal cleaning step was conducted at 1300 °C for 10 min. h-BN was then grown at 1400 °C with a gas flow rate of 6 m/s. All temperatures in this study were recorded by thermocouple readings. During this process, NH_3 was employed as the Group V precursor and TEB as the Group III precursor. The NH_3 flow rate was 89.2 mmol/min, while the TEB flow rate was 14.8 μmol/min. In the pulsed method, TEB was supplied first for 2 s, followed by NH_3 for 1 s. The purge time between NH_3 and TEB supply was 0 s. The number of pulse cycles for the BN nucleus and films was 40 and 600, respectively. H_2 was employed as the carrier gas. The growth pressure was maintained at 30 Torr.

4.3 Post-growth annealing of h-BN and AlN

The annealing apparatus employed combined an annealing furnace with a high-frequency induction heating power supply to control both the furnace atmosphere system and heating system, thereby facilitating the annealing process. Samples were positioned face-to-face, with the annealing atmosphere comprising nitrogen. h-BN and AlN were annealed at 1650 °C for 3 h. All temperatures in this study were recorded by thermocouple readings.

4.4 Characterizations

Atomic structure characterization and elemental analysis of h-BN and AlN layers were performed using a TEM (FEI; Talos F200X) and an aberration-corrected TEM (ACTEM, FEI; Themis Z) equipped with an EDS. TEM samples were prepared and thinned using a FIB (FEI; Helios 5 UX). HRXRD (Malvern Panalytical; X' Pert MRD Pro) was employed to analyse the crystalline quality and stress state of AlN, and the thickness of h-BN was also measured using this. Powder XRD (Malvern Panalytical; PW3040/60 X'Pert PRO) confirmed the crystalline orientation of h-BN and AlN. Raman spectroscopy (Nanophoton; RAMAN-11) recorded Raman spectra of h-BN and AlN template substrates. Surface topography of h-BN was obtained using AFM (Oxford Instruments; MFP-3D Origin+). Elemental composition and chemical state of h-BN were analyzed by XPS (ULVAC-PHI; Quantera SXM).

4.5 Computational method

The computational task of this paper was implemented using the first-principles calculation software PWmat. Atomic structure optimization and energy self-consistent calculations were performed using the Perdew–Burke–Ernzerhof (PBE) functional within the generalized gradient approximation (GGA) framework, with *k*-point settings of 2 × 2 × 1 and 6 × 6 × 1, respectively. The lattice constants for h-BN and AlN within the unit cell were determined to be 2.50 and 3.11 Å, respectively. A vacuum layer thickness of 30 Å was employed to prevent spurious interactions. The plane wave cutoff energy was set to 60 Rydberg (Ry; 816 eV), with a force convergence accuracy of 0.05 eV/Å. The van der Waals corrections were included to obtain an accurate description of interlayer interactions. The convergence criterion for the maximum force experienced by atoms during relaxation was set at 0.05 Å.

Electronic Supplementary Material: Supplementary material (the crystal quality of FFA Sp-AlN templates with different polarities, quantitative comparison of h-BN/AlN interfacial properties, MOVPE growth schematic, AFM images, HAADF-scanning TEM (STEM) images, Raman and XPS spectra, XRD characterizations, exfoliation-related results, and detailed DFT computational methodology) is available in the online version of this article at https://doi.org/10.26599/NR.2026.94908822.

Data availability

All data needed to support the conclusions in the paper are presented in the manuscript and the Electronic Supplementary Material. Additional data related to this paper may be requested from the corresponding author upon request.

Acknowledgements

This work was supported in part by Japan Society for the Promotion of Science Grants-in-Aid for Scientific Research (JSPS KAKENHI, No. 25K01680), Japan Science and Technology Agency Strategic International Collaborative Research Program (JST-SICORP, No. JPMJSC22C1), New Energy and Industrial Technology Development Organization(NEDO) Intensive Support for Young Promising Researchers (No. 21502153-0), and NEDO Leading Research Program.

Declaration of competing interest

All the contributing authors report no conflict of interests in this work.

Author contribution statement

Y. N. W.: Data curation, formal analysis, validation, visualization, writing – original draft. R. A.: Formal analysis, funding acquisition, writing – review & editing. K. T.: Data curation, methodology. T. T.: Methodology, investigation. H. Y.: Formal analysis, validation. W. T. Z.: Investigation, formal analysis. K. X.: Resources, methodology, formal analysis. H. M.: Conceptualization, supervision, resources, project administration, writing – review & editing, funding acquisition, methodology. All the authors have approved the final manuscript.

Use of AI statement

None.

References

[1] Cassabois, G.; Valvin, P.; Gil, B. Hexagonal boron nitride is an indirect bandgap semiconductor. *Nat. Photonics* **2016**, *10*, 262–266.

[2] Caldwell, J. D.; Aharonovich, I.; Cassabois, G.; Edgar, J. H.; Gil, B.; Basov, D. N. Photonics with hexagonal boron nitride. *Nat. Rev. Mater.* **2019**, *4*, 552–567.

[3] Zhang, S. J.; Tao, Y.; Qin, S. W.; Li, D.; Cao, K. K.; Lv, L.; Ma, G. K.; Rao, Y. H.; Wan, H. Z.; Hao, W. Memristors based on two-dimensional h-BN materials: Synthesis, mechanism, optimization and application. *npj 2D Mater. Appl.* **2024**, *8*, 81.

[4] Rhodes, D.; Chae, S. H.; Ribeiro-Palau, R.; Hone, J. Disorder in van der Waals heterostructures of 2D materials. *Nat. Mater.* **2019**, *18*, 541–549.

[5] Jang, A. R.; Hong, S.; Hyun, C.; Yoon, S. I.; Kim, G.; Jeong, H. Y.; Shin, T. J.; Park, S. O.; Wong, K.; Kwak, S. K. et al. Wafer-scale and wrinkle-free epitaxial growth of single-orientated multilayer hexagonal boron nitride on sapphire. *Nano Lett.* **2016**, *16*, 3360–3366.

[6] Chen, T. A.; Chuu, C. P.; Tseng, C. C.; Wen, C. K.; Wong, H. S. P.; Pan, S. Y.; Li, R. T.; Chao, T. A.; Chueh, W. C.; Zhang, Y. F. et al. Wafer-scale single-crystal hexagonal boron nitride monolayers on Cu (111). *Nature* **2020**, *579*, 219–223.

[7] Moon, S.; Kim, J.; Park, J.; Im, S.; Kim, J.; Hwang, I.; Kim, J. K. Hexagonal boron nitride for next-generation photonics and electronics. *Adv. Mater.* **2023**, *35*, 2204161.

[8] Lee, G. H.; Yu, Y. J.; Cui, X.; Petrone, N.; Lee, C. H.; Choi, M. S.; Lee, D. Y.; Lee, C.; Yoo, W. J.; Watanabe, K. et al. Flexible and transparent MoS_2 field-effect transistors on hexagonal boron nitride-graphene heterostructures. *ACS Nano* **2013**, *7*, 7931–7936.

[9] Britnell, L.; Gorbachev, R. V.; Jalil, R.; Belle, B. D.; Schedin, F.; Mishchenko, A.; Georgiou, T.; Katsnelson, M. I.; Eaves, L.; Morozov, S. V. et al. Field-effect tunneling transistor based on vertical graphene heterostructures. *Science* **2012**, *335*, 947–950.

[10] Doganov, R. A.; O'Farrell, E. C. T.; Koenig, S. P.; Yeo, Y.; Ziletti, A.; Carvalho, A.; Campbell, D. K.; Coker, D. F.; Watanabe, K.; Taniguchi, T. et al. Transport properties of pristine few-layer black phosphorus by van der Waals passivation in an inert atmosphere. *Nat. Commun.* **2015**, *6*, 6647.

[11] Vuong, P.; Sundaram, S.; Mballo, A.; Patriarche, G.; Leone, S.; Benkhelifa, F.; Karrakchou, S.; Moudakir, T.; Gautier, S.; Voss, P. L. et al. Control of the mechanical adhesion of III–V materials grown on layered h-BN. *ACS Appl. Mater. Interfaces* **2020**, *12*, 55460–55466.

[12] Kobayashi, Y.; Kumakura, K.; Akasaka, T.; Makimoto, T. Layered boron nitride as a release layer for mechanical transfer of GaN-based devices. *Nature* **2012**, *484*, 223–227.

[13] Kwak, H. M.; Kim, J.; Lee, J. S.; Kim, J.; Baik, J.; Choi, S. Y.; Shin, S.; Kim, J. S.; Mun, S. H.; Kim, K. P. et al. 2D-material-assisted GaN growth on GaN template by MOCVD and its exfoliation strategy. *ACS Appl. Mater. Interfaces* **2023**, *15*, 59025–59036.

[14] Park, J. H.; Yang, X.; Lee, J. Y.; Park, M. D.; Bae, S. Y.; Pristovsek, M.; Amano, H.; Lee, D. S. The stability of graphene and boron nitride for III-nitride epitaxy and post-growth exfoliation. *Chem. Sci.* **2021**, *12*, 7713–7719.

[15] Kim, H.; Liu, Y. P.; Lu, K. Y.; Chang, C. S.; Sung, D.; Akl, M.; Qiao, K.; Kim, K. S.; Park, B. I.; Zhu, M. L. et al. High-throughput manufacturing of epitaxial membranes from a single wafer by 2D materials-based layer transfer process. *Nat. Nanotechnol.* **2023**, *18*, 464–470.

[16] Shi, Y. M.; Meng, J. H.; Xia, Z. C.; Huang, J. D.; Liu, W. K.; Jiang, J.; Yin, Z. G.; Deng, J. X.; Zhang, X. W. Growth modes of β-Ga_2O_3 on h-BN: Remote epitaxy and van der Waals epitaxy. *Nano Res.* **2025**, *18*, 94907129.

[17] Wang, L. L.; Yang, S. Y.; Gao, Y. Q.; Yang, J. K.; Duo, Y.; Song, S.; Yan, J. C.; Wang, J. X.; Li, J. M.; Wei, T. B. Quasi-van der Waals epitaxy of a stress-released AlN film on thermally annealed hexagonal BN for deep ultraviolet light-emitting diodes. *ACS Appl. Mater. Interfaces* **2023**, *15*, 23501–23511.

[18] Liu, F.; Rong, X.; Yu, Y.; Wang, T.; Sheng, B. W.; Wei, J. Q.; Liu, S. F.; Yang, J. J.; Bertram, F.; Xu, F. J. et al. Thermally annealed wafer-scale h-BN films grown on sapphire substrate by molecular beam epitaxy. *Appl. Phys. Lett.* **2020**, *116*, 142104.

[19] Wang, L.; Xu, X. Z.; Zhang, L. N.; Qiao, R. X.; Wu, M. H.; Wang, Z. C.; Zhang, S.; Liang, J.; Zhang, Z. H.; Zhang, Z. B. et al. Epitaxial growth of a 100-square-centimetre single-crystal hexagonal boron nitride monolayer on copper. *Nature* **2019**, *570*, 91–95.

[20] Ma, K. Y.; Zhang, L. N.; Jin, S.; Wang, Y.; Yoon, S. I.; Hwang, H.; Oh, J.; Jeong, D. S.; Wang, M. H.; Chatterjee, S. et al. Epitaxial single-crystal hexagonal boron nitride multilayers on Ni (111). *Nature* **2022**, *606*, 88–93.

[21] Li, J. Z.; Samad, A.; Yuan, Y.; Wang, Q. X.; Hedhili, M. N.; Lanza, M.; Schwingenschlögl, U.; Abate, I.; Akinwande, D.; Liu, Z. et al. Single-crystal hBN monolayers from aligned hexagonal islands. *Nat. Commun.* **2024**, *15*, 8589.

[22] Li, X.; Sundaram, S.; El Gmili, Y.; Ayari, T.; Puybaret, R.; Patriarche, G.; Voss, P. L.; Salvestrini, J. P.; Ougazzaden, A. Large-area two-dimensional layered hexagonal boron nitride grown on sapphire by metalorganic vapor phase epitaxy. *Cryst. Growth Des.* **2016**, *16*, 3409–3415.

[23] Jeong, H.; Kim, D. Y.; Kim, J.; Moon, S.; Han, N. M.; Lee, S. H.; Okello, O. F. N.; Song, K.; Choi, S. Y.; Kim, J. K. Wafer-scale and selective-area growth of high-quality hexagonal boron nitride on Ni (111) by metal–organic chemical vapor deposition. *Sci. Rep.* **2019**, *9*, 5736.

[24] Chubarov, M.; Pedersen, H.; Högberg, H.; Darakchieva, V.; Jensen, J.; Persson, P. O. Å.; Henry, A. Epitaxial CVD growth of sp^2-hybridized boron nitride using aluminum nitride as buffer layer. *Phys. Status Solidi Rapid Res. Lett.* **2011**, *5*, 397–399.

[25] Tran, T. M.; Kassem, A.; Ottapilakkal, V.; Vuong, P.; Gujrati, R.; Bourras, M.; Srivastava, A.; Perepeliuc, A.; Moudakir, T.; Gautier, S. et al. Transferrable GaN-based Micro-LED heterostructures grown on h-BN for optogenetic applications. *J. Cryst. Growth* **2025**, *650*, 127979.

[26] Moon, S.; Chang, S. J.; Kim, Y.; Okello, O. F. N.; Kim, J.; Kim, J.; Jung, H. W.; Ahn, H. K.; Kim, D. S.; Choi, S. Y. et al. van der Waals heterostructure of hexagonal boron nitride with an AlGaN/GaN epitaxial wafer for high-performance radio frequency applications. *ACS Appl. Mater. Interfaces* **2021**, *13*, 59440–59449.

[27] Hao, G. D.; Tsuzuki, S.; Inoue, S. I. Small valence band offset of h-BN/$Al_{0.7}Ga_{0.3}N$ heterojunction measured by X-ray photoelectron spectroscopy. *Appl. Phys. Lett.* **2019**, *114*, 011603.

[28] Dąbrowska, A. K.; Tokarczyk, M.; Kowalski, G.; Binder, J.; Bożek, R.; Borysiuk, J.; Stępniewski, R.; Wysmołek, A. Two stage epitaxial growth of wafer-size multilayer h-BN by metal–organic vapor phase epitaxy—A homoepitaxial approach. *2D Mater.* **2020**, *8*, 015017.

[29] Yang, X.; Nitta, S.; Pristovsek, M.; Liu, Y. H.; Nagamatsu, K.;

Kushimoto, M.; Honda, Y.; Amano, H. Interface amorphization in hexagonal boron nitride films on sapphire substrate grown by metalorganic vapor phase epitaxy. *Appl. Phys. Express* **2018**, *11*, 051002.

[30] Yang, X.; Pristovsek, M.; Nitta, S.; Liu, Y. H.; Honda, Y.; Koide, Y.; Kawarada, H.; Amano, H. Epitaxial combination of two-dimensional hexagonal boron nitride with single-crystalline diamond substrate. *ACS Appl. Mater. Interfaces* **2020**, *12*, 46466–46475.

[31] Moon, S.; Okello, O. F. N.; Rousseau, A.; Choi, C. W.; Kim, Y.; Park, Y.; Kim, J.; Kim, J.; Kim, M.; Valvin, P. et al. Wafer-scale AA-stacked hexagonal boron nitride grown on a GaN substrate. *Nat. Mater.* **2025**, *24*, 843–851.

[32] Zdanowicz, E.; Herman, A. P.; Opołczyńska, K.; Gorantla, S.; Olszewski, W.; Serafińczuk, J.; Hommel, D.; Kudrawiec, R. Toward h-BN/GaN Schottky diodes: Spectroscopic study on the electronic phenomena at the interface. *ACS Appl. Mater. Interfaces* **2022**, *14*, 6131–6137.

[33] Yang, Q. C.; Liu, J. X.; Duo, Y.; Dong, J. N.; Huo, Z. Q.; Yang, J. K.; Ran, J. X.; Wang, J. X.; Gao, P.; Qi, J. J. et al. Highly oriented and wafer-scale exfoliation of h-BN grown on AlN by metalorganic chemical vapor deposition. *Appl. Phys. Lett.* **2025**, *126*, 132103.

[34] Yang, X.; Nitta, S.; Pristovsek, M.; Liu, Y. H.; Liao, Y. Q.; Kushimoto, M.; Honda, Y.; Amano, H. Scalable synthesis of multilayer h-BN on AlN by metalorganic vapor phase epitaxy: Nucleation and growth mechanism. *2D Mater.* **2020**, *7*, 015004.

[35] Wong, S. S.; Lin, Z. Y.; Ho, S. Z.; Hsu, C. E.; Li, P. H.; Chen, C. Y.; Huang, Y. F.; Chang, K. E.; Hsieh, Y. C.; Chen, C. H. et al. Epitaxial ferroelectric hexagonal boron nitride grown on graphene. *Adv. Mater.* **2025**, *37*, 2414442.

[36] Miyake, H.; Lin, C. H.; Tokoro, K.; Hiramatsu, K. Preparation of high-quality AlN on sapphire by high-temperature face-to-face annealing. *J. Cryst. Growth* **2016**, *456*, 155–159.

[37] Miyake, H.; Nishio, G.; Suzuki, S.; Hiramatsu, K.; Fukuyama, H.; Kaur, J.; Kuwano, N. Annealing of an AlN buffer layer in N_2–CO for growth of a high-quality AlN film on sapphire. *Appl. Phys. Express* **2016**, *9*, 025501.

[38] Tamano, T.; Shojiki, K.; Akiyama, T.; Akaike, R.; Nakamura, T.; Honda, H.; Sato, E.; Uemukai, M.; Tanikawa, T.; Katayama, R. et al. Analysis of inversion-domain boundaries in four-layer polarity-inverted AlN structure. *Appl. Phys. Lett.* **2025**, *126*, 032108.

[39] Namikawa, G.; Shojiki, K.; Yoshida, R.; Kusuda, R.; Uesugi, K.; Miyake, H. MOVPE growth of AlN and AlGaN films on N-polar annealed and sputtered AlN templates. *J. Cryst. Growth* **2023**, *617*, 127256.

[40] Tatarczak, P.; Iwański, J.; Dąbrowska, A. K.; Tokarczyk, M.; Binder, J.; Stępniewski, R.; Wysmołek, A. Strain modulation of epitaxial h-BN on sapphire: The role of wrinkle formation for large-area two-dimensional materials. *Nanotechnology* **2024**, *35*, 175703.

[41] Chugh, D.; Wong-Leung, J.; Li, L.; Lysevych, M.; Tan, H. H.; Jagadish, C. Flow modulation epitaxy of hexagonal boron nitride. *2D Mater.* **2018**, *5*, 045018.

[42] Tokarczyk, M.; Dąbrowska, A. K.; Kowalski, G.; Bożek, R.; Iwański, J.; Binder, J.; Stępniewski, R.; Wysmołek, A. Effective substrate for the growth of multilayer h-BN on sapphire-substrate off-cut, pre-growth, and post-growth conditions in metal–organic vapor phase epitaxy. *2D Mater.* **2023**, *10*, 025010.

[43] Zhang, Q.; Guo, Y. N.; Liu, Z. B.; Wang, D. D.; Li, Q.; Yan, J. C.; Li, J. C.; Wang, J. X. Effect of the growth interruption on the surface morphology and crystalline quality of MOCVD-grown h-BN. *Crystals* **2023**, *13*, 486.

[44] Binder, J.; Dabrowska, A. K.; Tokarczyk, M.; Ludwiczak, K.; Bozek, R.; Kowalski, G.; Stepniewski, R.; Wysmolek, A. Epitaxial hexagonal boron nitride for hydrogen generation by radiolysis of interfacial water. *Nano Lett.* **2023**, *23*, 1267–1272.

[45] Silvi, B.; Savin, A. Classification of chemical bonds based on topological analysis of electron localization functions. *Nature* **1994**, *371*, 683–686.

[46] Uesugi, K.; Hayashi, Y.; Shojiki, K.; Xiao, S. Y.; Nagamatsu, K.; Yoshida, H.; Miyake, H. Fabrication of AlN templates on SiC substrates by sputtering-deposition and high-temperature annealing. *J. Cryst. Growth* **2019**, *510*, 13–17.

[47] Wang, D.; Uesugi, K.; Xiao, S. Y.; Norimatsu, K.; Miyake, H. Low dislocation density AlN on sapphire prepared by double sputtering and annealing. *Appl. Phys. Express* **2020**, *13*, 095501.

[48] Ben, J. W.; Sun, X. J.; Jia, Y. P.; Jiang, K.; Shi, Z. M.; Liu, H. N.; Wang, Y.; Kai, C. H.; Wu, Y.; Li, D. B. Defect evolution in AlN templates on PVD-AlN/sapphire substrates by thermal annealing. *CrystEngComm* **2018**, *20*, 4623–4629.

[49] Yang, X.; Pristovsek, M.; Nitta, S.; Honda, Y.; Ohtake, A.; Sakuma, Y.; Hiroto, T.; Ishida, T.; Ikezawa, M.; Guo, Q. X. et al. Highly oriented epitaxial hexagonal boron nitride multilayers on high-temperature-resistant single-crystal aluminum nitride (0001). *Adv. Sci.* **2025**, *12*, e09354.

[50] Chen, J. R.; Wang, G. K.; Meng, J. H.; Cheng, Y.; Yin, Z. G.; Tian, Y.; Huang, J. D.; Zhang, S. Y.; Wu, J. L.; Zhang, X. W. Low-temperature direct growth of few-layer hexagonal boron nitride on catalyst-free sapphire substrates. *ACS Appl. Mater. Interfaces* **2022**, *14*, 7004–7011.

[51] Yang, P. L.; Moon, S.; Im, S.; Kim, J.; Song, J.; Ji, C.; Pak, S.; Hao, Z. B.; Luo, Y.; Sun, C. Z. et al. Self-exfoliation in quasi-van der Waals epitaxy of III-nitrides on hexagonal boron nitride. *ACS Appl. Electron. Mater.* **2025**, *7*, 9380–9388.

[52] Zaiter, A.; Michon, A.; Nemoz, M.; Courville, A.; Vennéguès, P.; Ottapilakkal, V.; Vuong, P.; Sundaram, S.; Ougazzaden, A.; Brault, J. Crystalline quality and surface morphology improvement of face-to-face annealed MBE-grown AlN on h-BN. *Materials* **2022**, *15*, 8602.

[53] Jung, J. H.; Park, C. H.; Ihm, J. A rigorous method of calculating exfoliation energies from first principles. *Nano Lett.* **2018**, *18*, 2759–2765.

This is an open access article under the terms of the Creative Commons Attribution 4.0 International License (CC BY 4.0, https://creativecommons.org/licenses/by/4.0/).

© The Author(s) 2026. Published by Tsinghua University Press.